Supplementary Information for

Spin-Selective Charge Transfer Pathways in Photoexcited Helicene-Perylenediiimide Dyads

Giulia Agnoloni,[a] Angelo Carella,[b,c] Jakob Staab,[a] Maksim Arsentev,[a] Michela Lupi,[a] Stefano Menichetti,[a] Caterina Viglianisi,[a] Ryan M. Young,[c] Federico Totti,[a] Michael R. Wasielewski,[c]* Alberto Privitera,[b,c]* and Roberta Sessoli[a]*

[a] *Department of Chemistry "U. Schiff", University of Florence & UdR INSTM Firenze, 50019, Sesto Fiorentino, Italy.*

[b] *Department of Industrial Engineering, University of Florence & UdR INSTM Firenze, 50139, Firenze, Italy*

[c] *Department of Chemistry, Center for Molecular Quantum Transduction, and Institute for Quantum Information Research and Engineering, Northwestern University, 60208-3113, Evanston, IL (USA)*

Table of Contents

S1. Materials, synthesis, and characterization

Materials. ^{1}H and ^{13}C NMR spectra were recorded with *Varian MercuryPlus 400* and *Varian Inova 400*, using $CDCl_3$ and $(CD_3)_2CO$ as solvents. Residual $CHCl_3$ at δ = 7.26 ppm and CD_3COCD_2H at δ = 2.05 ppm were used as internal references for ^{1}H NMR spectra; central line of $CDCl_3$ at δ = 77.16 ppm and $(CD_3)_2CO$ at δ = 30.60 were used as internal references for ^{13}C NMR spectra. Fourier-transformed infrared (FT-IR) spectra were recorded with a *PerkinElmer SpectrumTwo* spectrometer. Electrospray ionization mass spectra (ESI-MS) were recorded with *LC-MS LCQ Fleet ThermoFisher Scientific* instrument. Melting points were measured with a *Stuart SMP50 Automatic Melting Point Apparatus*. Thin-layer chromatography (TLC) on commercially available precoated plates (silica gel 60 F_{254}) were used to monitor the reactions, and the products were visualized with acidic vanillin solution. Column chromatography was performed using Silica gel 60 (230–400 mesh). Dry solvents were obtained from a *PureSolv Micro Solvent Purification System*. Elemental analyses were performed on a *ThermoScientific FlashSmart CHNS/O Analyzer*.

Synthesis and characterization. The synthesis and characterization of all the donor-acceptor dyads are described in detail below. All chemicals were obtained from commercial suppliers and used as received without further purification. $Pd(PPh_3)Cl_2$, $Pd(PPh_3)_4$, and triflic anhydride were stored under nitrogen; triethylamine (TEA) and pyridine were freshly distilled over KOH before use. The synthesis of PMI (**10**), Helicene **6**, 4-((4-ethynylphenyl)ethynyl)aniline, and **Dyad 3** are described elsewhere.[1]

Synthesis of the bridge

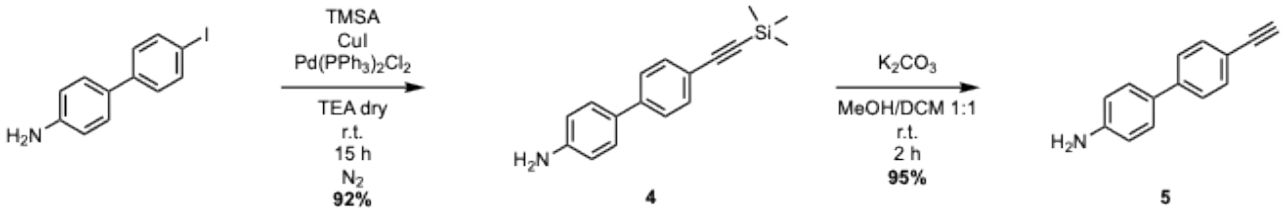

Figure S1. Synthesis of **4'-ethynyl-[1,1'-biphenyl]-4-amine** (**5**).

4'-((trimethylsilyl)ethynyl)-[1,1'-biphenyl]-4-amine (4). A dry Schlenk tube was charged with 4'-iodo-[1,1'-biphenyl]-4-amine (200 mg, 0.678 mmol, 1 eq), $Pd(PPh_3)_2Cl_2$ (14 mg, 0.02 mmol, 0.03 eq), CuI (6 mg, 0.03 mmol, 0.05 eq). Three vacuum-nitrogen cycles were performed, and through syringe TMSA (0.113 mL, 0.813 mmol, 1.2 eq) and dry and degassed triethylamine (3.3 mL) were added. The reaction mixture was stirred under nitrogen flux at room temperature for 17 h. The mixture was diluted with EtOAc and washed with NH_4Cl, H_2O, and brine. The organic layer was collected and the volatiles removed via rotary evaporation. The crude product was purified by flash

chromatography on silica gel with hexane : ethyl acetate (1 : 1), to afford the product **4** (165 mg) with a yield of 92%. **^{1}H NMR** (200 MHz, $CDCl_3$, δ): 7.48 (s, 4H), 7.44-7.39 (d, 2H), 6.77-6.73 (d, 2H), 3.76 (s, 2H), 0.26 (s, 9H), ppm coincide with the literature.[2]

4'-ethynyl-[1,1'-biphenyl]-4-amine (5). A round-bottom flask was charged with **4** (165 mg, 0.62 mmol, 1 eq), K2CO3 (430 mg, 3.11 mmol, 5 eq), MeOH (4.2 mL), and DCM (4.2 mL). The reaction mixture was stirred under nitrogen atmosphere at room temperature for 2 h. The reaction was quenched with H_2O and then diluted with DCM. The organic layer was collected and the volatiles removed via rotary evaporation. Without further purification, compound **5** (114 mg) was obtained with a yield of 95%. **^{1}H NMR** (200 MHz, $CDCl_3$, δ): 7.51 (s, 4H), 7.44-7.39 (d, 2H), 6.78-6.74 (d, 2H), 3.77 (s, 2H), ppm coincide with the literature.[2]

Synthesis of the donor-bridge units

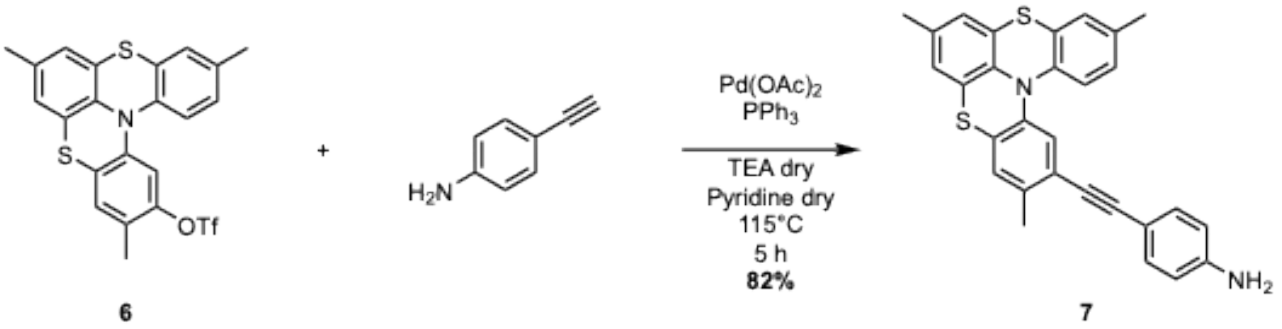

Figure S2. Synthesis of the helicene **7**.

Helicene 7. A Schlenk tube was charged with **6** (45 mg, 0.1 mmol, 1 eq), 4-ethynylaniline (32 mg, 0.18 mmol, 1.8 eq), PPh_3 (34 mg, 0.13 mmol, 1.3 eq) and $Pd(OAc)_2$ (1.1 mg, 0.005 mmol, 0.05 eq). Three vacuum-nitrogen cycles were performed, and through syringe dry and degassed triethylamine (0.5 mL) and pyridine (5 mL) were added. The mixture was stirred at 115°C for 5 hours. The suspension was diluted with DCM and washed with water. The organic layer was collected, dried over Na_2SO_4, filtered, and the volatiles were removed via rotary evaporation. The crude was purified by flash chromatography on silica gel with hexane : DCM (1 : 3) to obtain **7** (38 mg) as a yellow solid (82% yield). **^{1}H NMR** (400 MHz, $(CD_3)_2CO$, δ): 7.23-7.21 (d, 2H), 7.16-7.13 (m, 2H), 7.11-7.09 (m, 2H), 7.07-7.06 (m, 1H), 6.90 (m, 2H), 6.66-6.64 (d, 2H), 5.07 (m, 2H), 2.41 (s, 3H), 2.30 (s, 3H), 2.23 (s, 3H), ppm. **^{13}C NMR** (100 MHz, $(CD_3)_2CO$, δ): 150.20, 141.28, 140.63, 137.76, 136.54, 135.96, 135.59, 133.53, 129.43, 129.26, 128.98, 127.48, 127.10, 126.97, 126.86, 126.37, 126.07, 124.21, 122.89, 121.07, 114.86, 110.87, 96.89, 85.54, 20.59, 20.28, 20.02, ppm. **Melting Point**:

139°C. **IR** (ATR neat) ν = 3472, 3375, 3211, 3030, 2917, 2854, 2200, 1618, 1514, 1484, 1449, 824 cm^{-1}. **Anal.** calcd for $C_{29}H_{22}N_2S_2$: C, 75.29; H, 4.79; N, 6.06; S, 13.86. Found: C, 75.19; H, 5.02; N, 5.55; S, 13.03. **ESI-MS**: 463.17 $(M+H)^+$; 925.08 $(2M+H)^+$; 946.58 $(2M+Na)^+$.

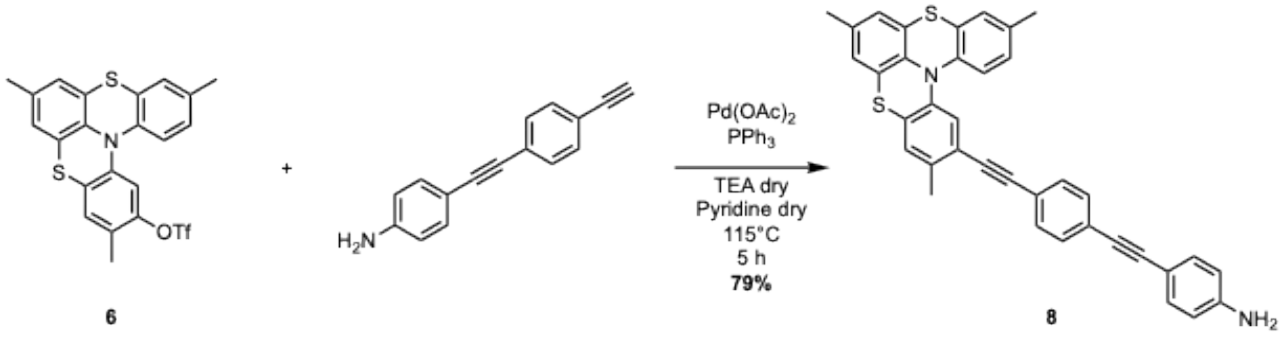

Figure S3. Synthesis of the helicene **8**.

Helicene 8. A Schlenk tube was charged with **6** (100 mg, 0.2 mmol, 1 eq), 4-((4-ethynylphenyl)ethynyl)aniline (78 mg, 0.36 mmol, 1.8 eq) , PPh_3 (68 mg, 0.26 mmol, 1.3 eq) and $Pd(OAc)_2$ (2.25 mg, 0.01 mmol, 0.05 eq). Three vacuum-nitrogen cycles were performed, and through syringe dry and degassed triethylamine (1 mL) and pyridine (10 mL) were added. The mixture was stirred at 115°C for 5 hours. The suspension was diluted with DCM and washed with water. The organic layer was collected, dried over Na_2SO_4, filtered, and the volatiles were removed via rotary evaporation. The crude was purified by flash chromatography on silica gel with DCM to obtain **8** (89 mg) as a yellow solid (79% yield). **^{1}H NMR** (400 MHz, $CDCl_3$, δ): 7.44-7.43 (dd, 4H), 7.35-7.32 (d, 2H), 7.28 (s, 1H), 7.10-7.08 (m, 1H), 7.05-7.02 (m, 2H), 6.96-6.94 (m, 1H), 6.79-6.77 (m, 2H), 6.64-6.62 (d, 2H), 3.83 (s, 2H), 2.44 (s, 3H), 2.30 (s, 3H), 2.21 (s, 3H), ppm. **^{13}C NMR** (100 MHz, $CDCl_3$, δ): 146.97, 140.55, 140.03, 137.09, 136.25, 134.69, 134.44, 133.14, 131.43, 131.34, 128.53, 128.46, 128.29, 127.79, 126.81, 126.29, 126.08, 125.68, 125.14, 123.97, 123.02, 122.41, 122.06, 120.33, 114.86, 112.41, 93.97, 92.40, 89.51, 87.33, 20.76, 20.50, 20.07, ppm. **Melting Point**: 156°C. **IR** (ATR neat) ν = 3475, 3380, 3206, 3035, 2916, 2852, 2206, 1618, 1518, 1483, 1450, 1278, 827 cm^{-1}. **Anal.** calcd for $C_{37}H_{26}N_2S_2$: C, 78.97; H, 4.66; N, 4.98; S, 11.39. Found: C, 78.92; H, 4.68; N, 4.81; S, 10.87. **ESI-MS**: 563.20 $(M+H)^+$.

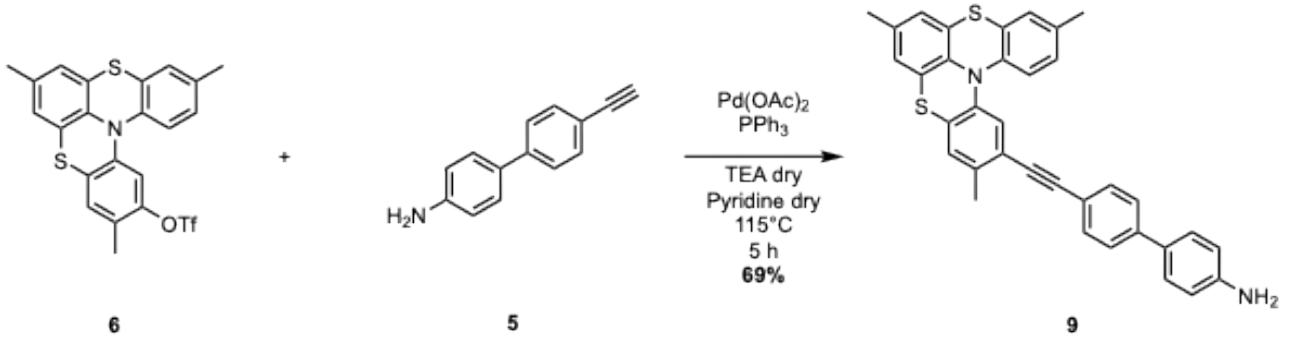

Figure S4. Synthesis of the helicene **9**.

Helicene 9. A Schlenk tube was charged with **6** (157 mg, 0.32 mmol, 1 eq), **5** (110 mg, 0.57 mmol, 1.8 eq), PPh_3 (109 mg, 0.41 mmol, 1.3 eq) and $Pd(OAc)_2$ (3.6 mg, 0.016 mmol, 0.05 eq). Three vacuum-nitrogen cycles were performed, and through syringe dry and degassed triethylamine (1 mL) and pyridine (10 mL) were added. The mixture was stirred at 115°C for 5 hours. The suspension was diluted with DCM and washed with water. The organic layer was collected, dried over Na_2SO_4, filtered, and the volatiles were removed via rotary evaporation. The crude was purified by flash chromatography on silica gel with DCM to obtain **9** (119 mg) as a yellow solid (69% yield). **^{1}H NMR** (400 MHz, $CDCl_3$, δ): 7.50 (s, 4H), 7.43-7.41 (d, 2H), 7.29 (s, 1H), 7.11-7.09 (m, 1H), 7.05-7.02 (m, 2H), 6.97-6.95 (m, 1H), 6.80-6.78 (m, 2H), 6.76-6.74 (d, 2H), 3.76 (s, 2H), 2.45 (s, 3H), 2.30 (s, 3H), 2.21 (s, 3H), ppm. **^{13}C NMR** (100 MHz, $CDCl_3$, δ): 146.37, 141.11, 140.53, 140.11, 137.16, 136.24, 134.67, 134.42, 131.95, 128.50, 128.48, 128.29, 128.03, 126.28, 126.24, 126.10, 125.70, 125.22, 123.02, 121.02, 120.38, 115.51, 94.33, 88.21, 20.77, 20.51, 20.11, ppm. **Melting Point**: 159°C. **IR** (ATR neat) ν = 3475, 3374, 3208, 3028, 2916, 2204, 1884, 1752, 1618, 1489, 1449, 1277, 814 cm^{-1}. **Anal.** calcd for $C_{35}H_{26}N_2S_2$: C, 78.03; H, 4.86; N, 5.20; S, 11.90. Found: C, 78.18; H, 4.90; N, 5.17; S, 11.67. **ESI-MS**: 539.24 $(M+H)^+$; 1077.74 $(2M+H)^+$.

Synthesis of the chiral donor-acceptor dyads

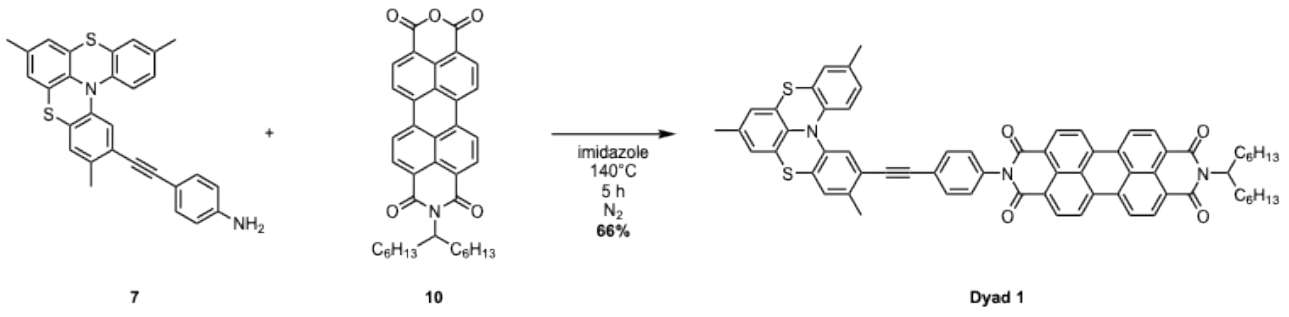

Figure S5. Synthesis of the dyad **1**.

Dyad 1. A round-bottom flask was charged with **10** (28 mg, 0.048 mmol, 1 eq), **7** (33 mg, 0.07 mmol, 1.5 eq), and imidazole (156 mg, 2.29 mmol, 32 eq). The reaction mixture was stirred at 140°C for 5 h, under nitrogen flux. Once cooled to room temperature, NH_4Cl was added to the mixture, and left stirring for 1 h. The mixture was then diluted with DCM and washed with H_2O. The organic layer was collected, dried over Na_2SO_4, filtered, and the volatiles were removed via rotary evaporation. The crude was purified by flash chromatography on silica gel with Petroleum Ether : DCM (1 : 2) and then DCM after removed the starting material, to obtain **dyad 1** (32 mg) as a red solid (66% yield). **^{1}H NMR** (400 MHz, $CDCl_3$, δ): 8.67-8.58 (m, 8H), 7.66-7.64 (m, 2H), 7.34-7.32 (m, 2H), 7.10-7.08 (m, 1H), 7.02 (m, 2H), 6.97-6.95 (m, 1H), 6.79-6.77 (m, 2H), 5.18 (m, 1H), 2.43 (s, 3H), 2.30-2.22 (m, 8H), 1.89 (m, 2H), 1.33-1.24 (m, 16H), 0.83 (t, 6H), ppm. **^{13}C NMR** (100 MHz, $CDCl_3$, δ): 163.43, 140.43, 140.05, 137.03, 136.39, 135.14, 134.96, 134.77, 134.51, 134.13, 132.55, 131.82, 129.76, 129.49, 128.98, 128.54, 128.45, 128.33, 126.77, 126.33, 126.16, 125.68, 125.11, 123.35, 123.13, 120.28, 93.52, 88.77, 55.01, 32.52, 31.93, 29.38, 27.15, 22.75, 20.78, 20.54, 20.11, 14.20, ppm. **Melting Point**: 210°C. **IR** (ATR neat) ν = 2951, 2923, 2854, 2161, 1697, 1654, 1593, 1338, 1251, 809, cm^{-1}. **Anal.** calcd for $C_{66}H_{55}N_3O_4S_2$: C, 77.85; H, 5.44; N, 4.13; O, 6.28; S, 6.30. Found: C, 77.68; H, 5.52; N, 4.12; O, 6.55; S, 6.13. **ESI-MS**: 1017.33 $(M)^{\bullet-}$.

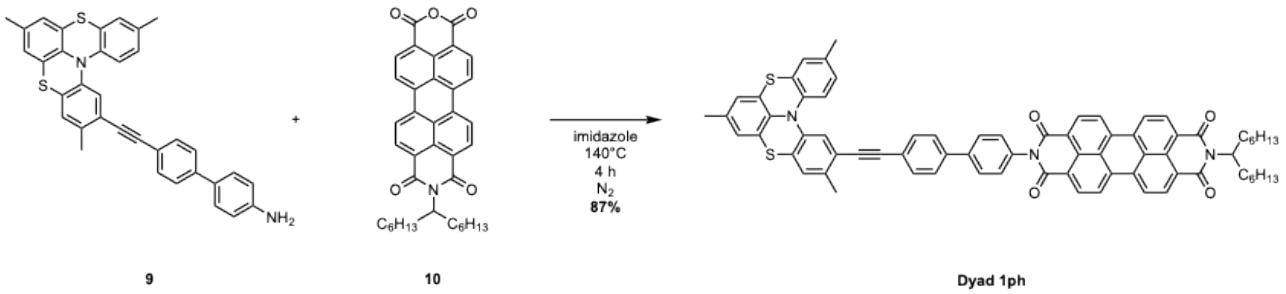

Figure S6. Synthesis of the dyad **1ph**.

Dyad 1ph. A round-bottom flask was charged with **10** (50 mg, 0.087 mmol, 1 eq), **9** (56 mg, 0.105 mmol, 1.2 eq), and imidazole (290 mg, 4.2 mmol, 48 eq). The reaction mixture was stirred at 140°C for 5 h, under nitrogen flux. Once cooled to room temperature, NH_4Cl was added to the mixture, and left stirring for 1 h. The mixture was then diluted with DCM and washed with H_2O. The organic layer was collected, dried over Na_2SO_4, filtered, and the volatiles were removed via rotary evaporation. The crude was purified by flash chromatography on silica gel with DCM to obtain **dyad 1ph** (68 mg) as a red solid (71% yield). **^{1}H NMR** (400 MHz, $CDCl_3$, δ): 8.75-8.64 (m, 8H), 7.79-7.77 (m, 2H), 7.62-7.58 (dd, 4H), 7.44-7.42 (m, 2H), 7.28 (m, 1H), 7.11-6.95 (m, 4H), 6.80-6.77 (m, 2H), 5.19 (m,

1H), 2.45 (s, 3H), 2.30-2.22 (m, 8H), 1.89 (m, 2H), 1.33-1.24 (m, 16H), 0.83 (t, 6H), ppm. **^{13}C NMR** (100 MHz, $CDCl_3$, δ): 163.76, 141.13, 140.54, 140.35, 140.11, 137.13, 136.31, 135.37, 134.69, 134.49, 132.12, 132.06, 130.01, 129.69, 129.21, 128.51, 128.34, 128.26, 127.40, 126.85, 126.33, 126.13, 125.72, 125.19, 123.50, 123.37, 123.22, 123.08, 122.69, 122.21, 120.37, 93.93, 88.84, 54.99, 32.53, 31.92, 29.37, 27.71, 22.74, 20.79, 20.53, 20.13, 14.20, ppm. **Melting Point**: 225°C. **IR** (ATR neat) ν = 3035, 2952, 2922, 2852, 2220, 1696, 1655, 1593, 1339, 1252, 810, cm^{-1}. **Anal.** calcd for $C_{72}H_{59}N_3O_4S_2$: C, 79.02; H, 5.43; N, 3.84; O, 5.85; S, 5.86. Found: C, 79.36; H, 5.30; N, 3.71; O, 6.15; S, 5.48. **ESI-MS**: 1093.34 $(M)^{\bullet-}$.

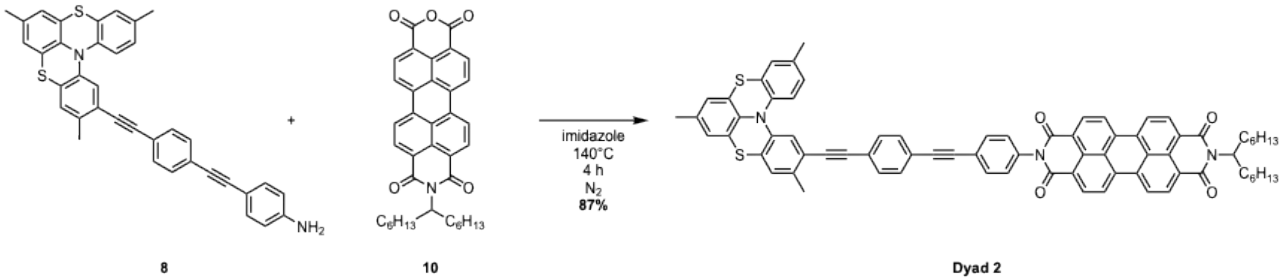

Figure S7. Synthesis of the dyad **2**.

Dyad 2. A round-bottom flask was charged with **10** (39 mg, 0.067 mmol, 1 eq), **8** (45 mg, 0.081 mmol, 1.2 eq), and imidazole (146 mg, 2.14 mmol, 32 eq). The reaction mixture was stirred at 140°C for 5 h, under nitrogen flux. Once cooled to room temperature, NH_4Cl was added to the mixture, and left stirring for 1 h. The mixture was then diluted with DCM and washed with H_2O. The organic layer was collected, dried over Na_2SO_4, filtered, and the volatiles were removed via rotary evaporation. The crude was purified by flash chromatography on silica gel with DCM to obtain **dyad 2** (65 mg) as a red solid (87% yield). **^{1}H NMR** (400 MHz, $CDCl_3$, δ): 8.66-8.55 (m, 8H), 7.73-7.71 (m, 2H), 7.52-7.43 (dd, 4H), 7.36-7.34 (m, 2H), 7.21 (s, 1H), 7.07-6.99 (m, 4H), 6.78-6.75 (d, 2H), 5.19 (m, 1H), 2.41 (s, 3H), 2.30-2.21 (m, 8H), 1.90 (m, 2H), 1.25 (m, 16H), 0.84 (t, 6H), ppm. **^{13}C NMR** (100 MHz, $CDCl_3$, δ): 163.48, 140.48, 140.04, 137.03, 136.26, 135.26, 135.14, 134.75, 134.49, 134.24, 132.74, 131.91, 131.79, 131.53, 129.87, 129.57, 129.01, 128.49, 128.47, 128.33, 127.89, 126.85, 126.70, 126.41, 126.32, 126.11, 125.69, 125.11, 123.94, 123.41, 123.36, 123.19, 123.14, 123.04, 121.92, 120.31, 93.77, 90.81, 90.20, 89.87, 55.01, 32.53, 31.92, 29.38, 27.13, 22.74, 20.78, 20.53, 20.08, 14.20, ppm. **Melting Point**: 212°C. **IR** (ATR neat) ν = 2950, 2922, 2857, 2154, 1697, 1658, 1593, 1339, 1252, 809, cm^{-1}. **Anal.** calcd for $C_{74}H_{59}N_3O_4S_2$: C, 79.47; H, 5.32; N, 3.76; O, 5.72; S, 5.73. Found: C, 79.20; H, 5.57; N, 3.62; O, 6.08; S, 5.53. **ESI-MS**: 1117.56 $(M)^{\bullet-}$.

S2. HPLC and Circular Dichroism Spectroscopy

Experimental HPLC Analytical (250 × 4.6 mm/ 5 µm) column packed with CHIRALPAK® IA chiral stationary phase was purchased from Chiral Technologies Europe. The HPLC resolution of products was performed with HPLC Semipreparative (250 x 10 mm/ 5 µm) column packed with CHIRALPAK® IG chiral stationary phase, purchased from Chiral Technologies Europe, on a HPLC Waters Alliance 2695 equipped with a 200 µL loop injector and a spectrophotometer UV Waters PDA 2996. The mobile phase, delivered at a flow rate of 1.5 mL/min, was hexane : DCM : IPA = 50 : 50 : 3 for **dyads 1**, **1ph**, and **2**, while the mixture hexane : DCM : IPA = 50 : 50 : 4 was used for **dyad 3**.

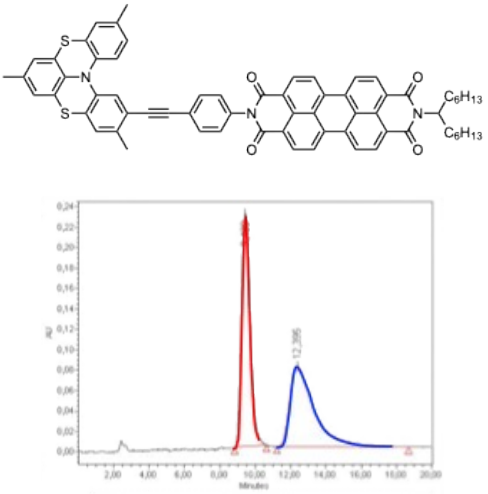

Figure S8. HPLC chromatogram of the racemic mixture of **dyad 1**.

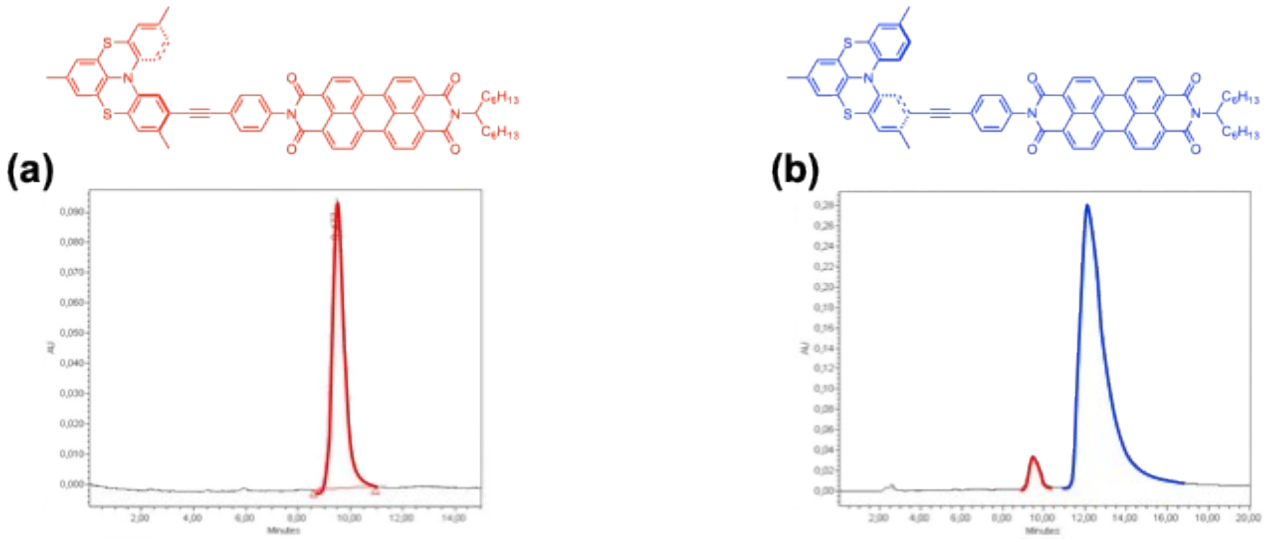

Figure S9. (a) HPLC chromatogram of (*P*)-**1** (enantiomeric excess 100%). (b) HPLC chromatogram of (*M*)-**1** (enantiomeric excess 92%).

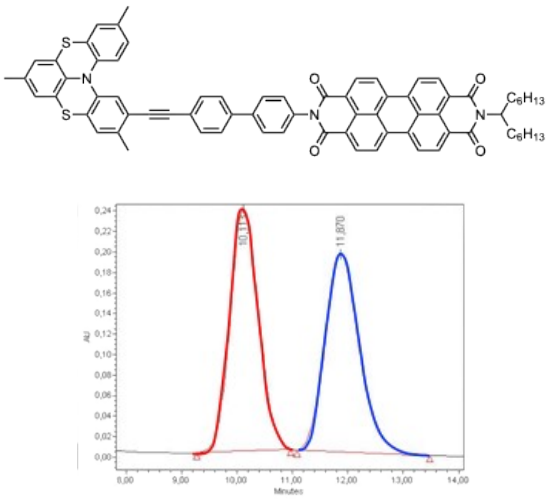

Figure S10. HPLC chromatogram of the racemic mixture of **dyad 1ph**.

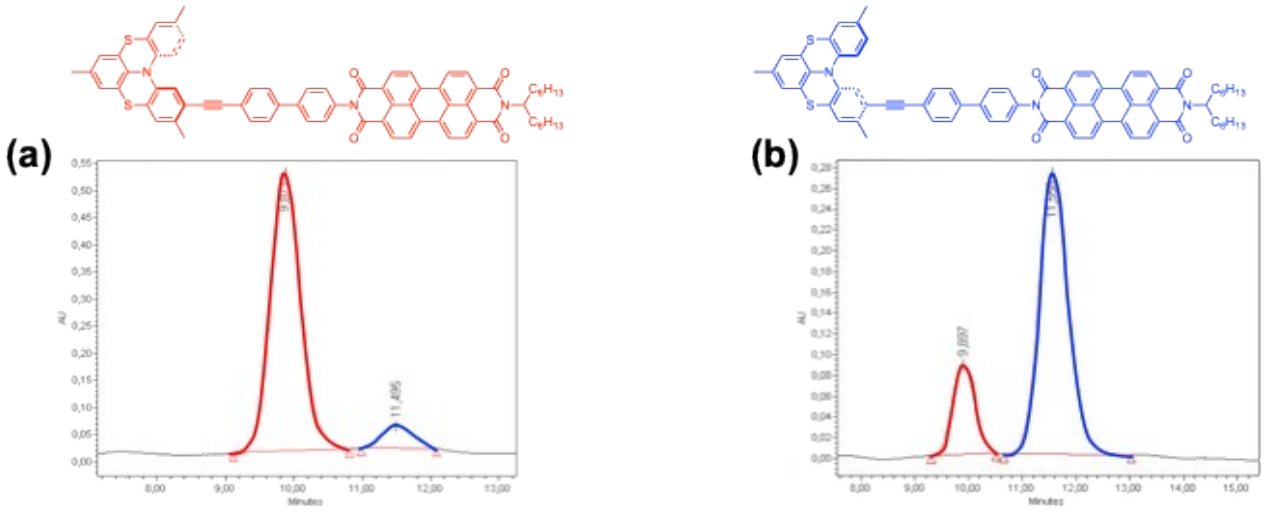

Figure S11. (a) HPLC chromatogram of (*P*)-**1ph** (enantiomeric excess 84%). (b) HPLC chromatogram of (*M*)-**1ph** (enantiomeric excess 60%).

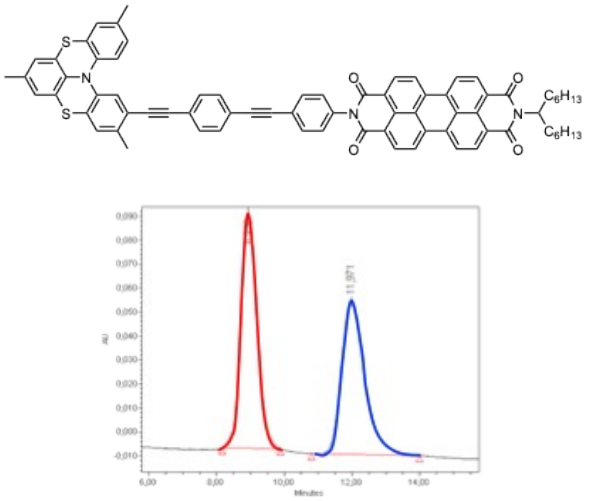

Figure S12. HPLC chromatogram of the racemic mixture of **dyad 2**.

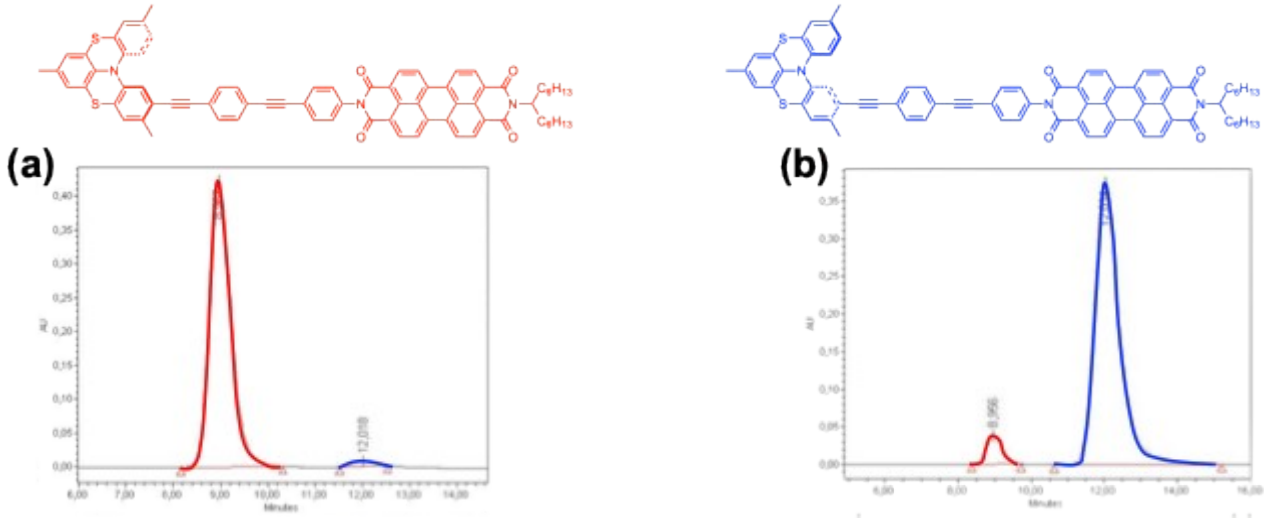

Figure S13. (a) HPLC chromatogram of (*P*)-**2** (enantiomeric excess 96%). (b) HPLC chromatogram of (*M*)-**2** (enantiomeric excess 88%).

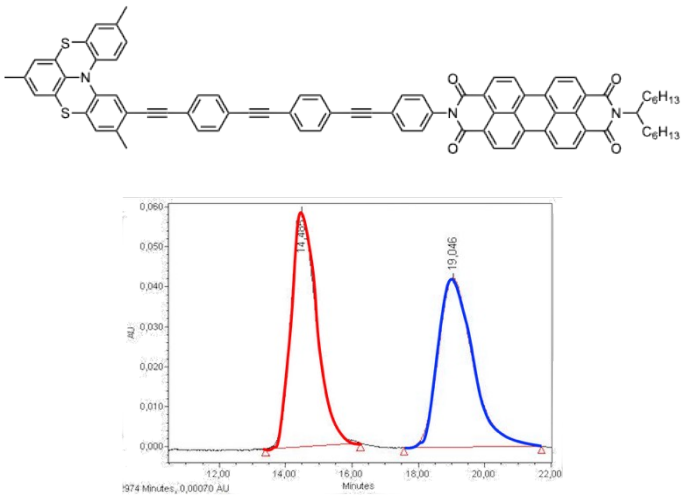

Figure S14. HPLC chromatogram of the racemic mixture of **dyad 3**.

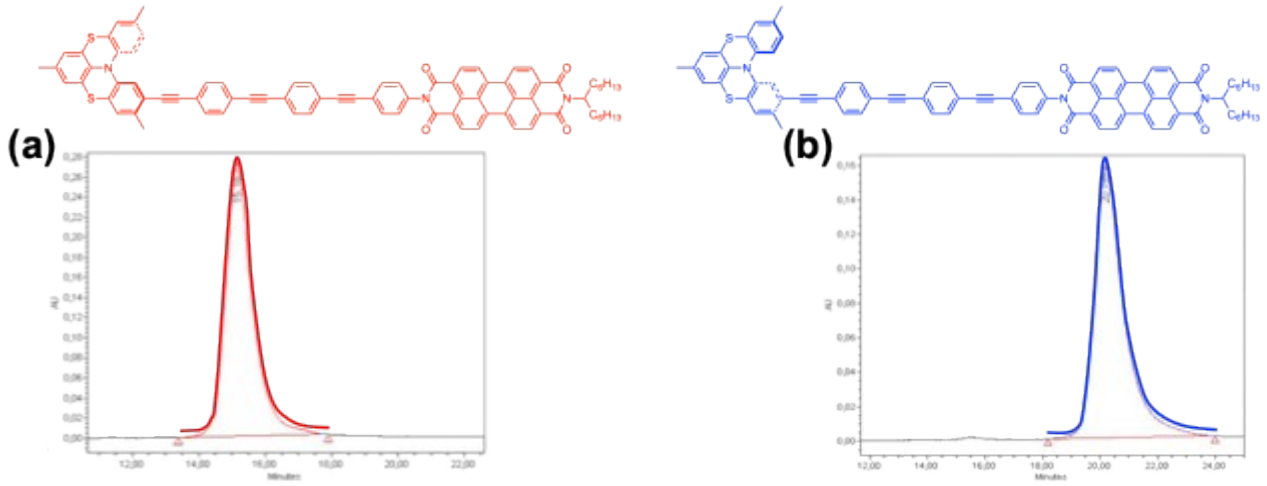

Figure S15. (a) HPLC chromatogram of (*P*)-**3** (enantiomeric excess 100%). (b) HPLC chromatogram of (*M*)-**3** (enantiomeric excess 100%).

Circular Dichroism (CD) spectra were recorded using the J-1500 Circular Dichroism Spectrophotometer, in DCM ($2.4x10^{-5}$M).

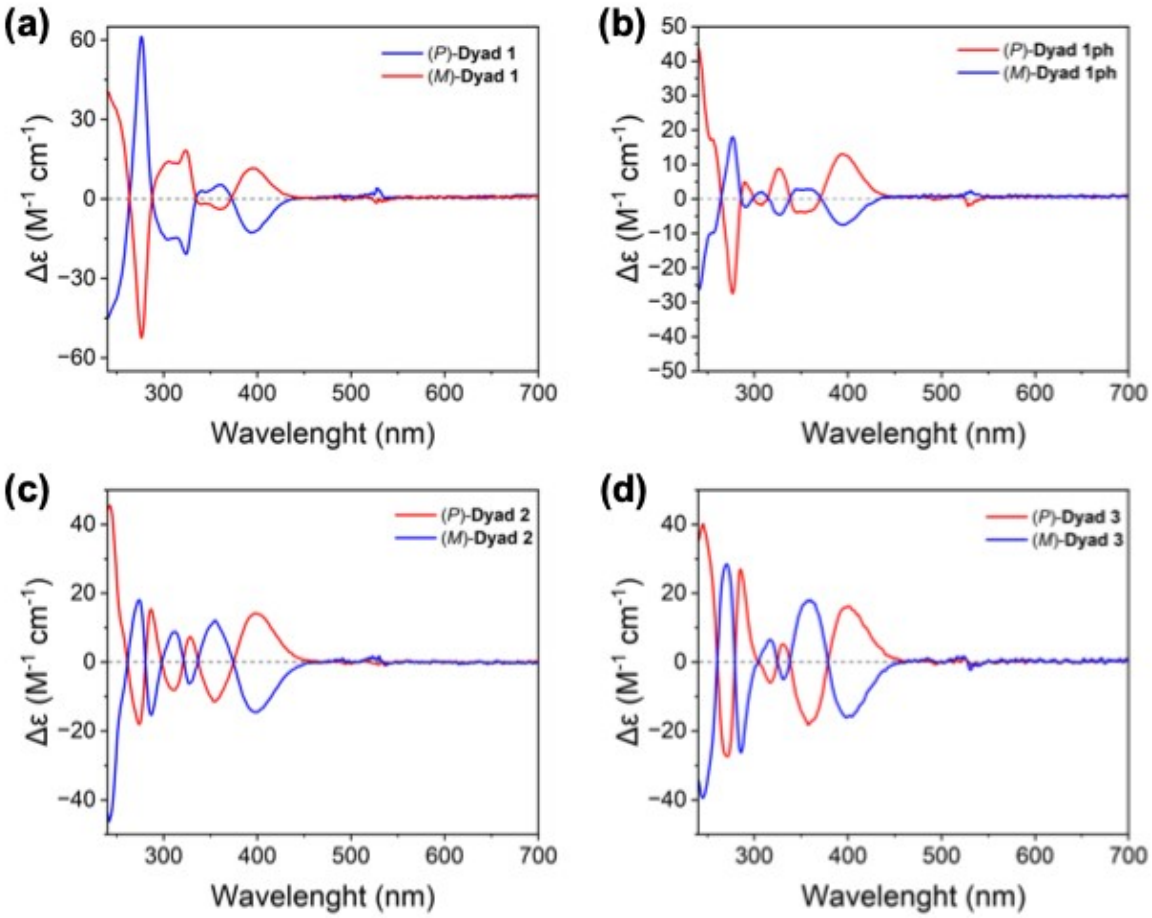

Figure S16. (a) CD spectra of (*P*)- and (*M*)-**1**. (b) CD spectra of (*P*)- and (*M*)-**1ph**. (c) CD spectra of (*P*)- and (*M*)-**2**. (d) CD spectra of (*P*)- and (*M*)-**3**.

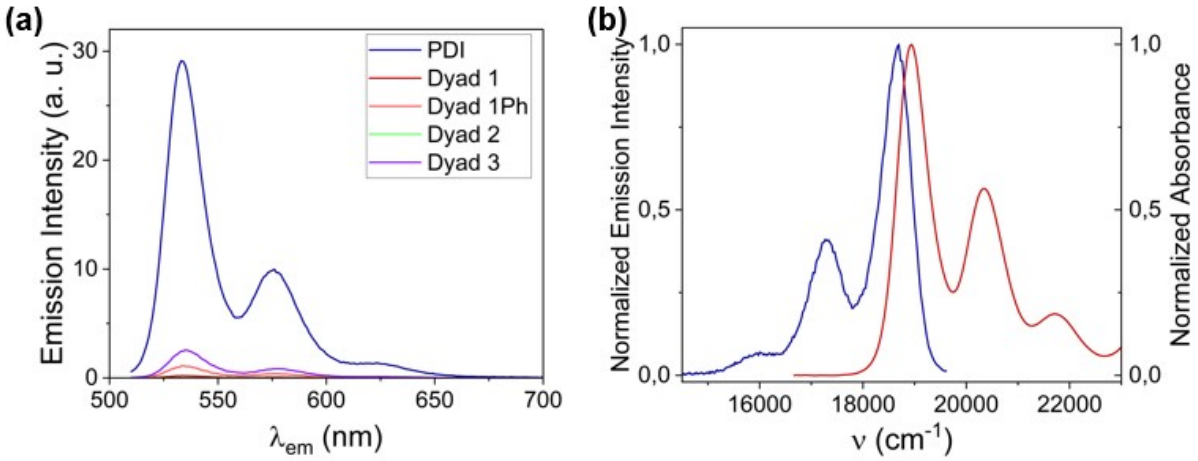

Figure S17. (a) Emission spectra of the dyads and PDI upon excitation at 530 nm, all emission spectra are measured using the same experimental conditions. (b) Normalized absorption (red) and emission (blue) spectra of **dyad 3** in toluene.

S3. DFT calculations

All electronic structure calculations were carried out within the Kohn-Sham (KS) formulation of density functional theory (DFT) implemented in the ORCA 6.0.0 package.[3,4] The CAM-B3LYP[5] exchange correlation functional was employed along with the D3BJ dispersion correction[6] and a polarizable continuum model (PCM) to account for electrostatic (ε = 2.3870, n = 1.4961, dielectric constant and refractive index, respectively) and cavity effects of the toluene solvent environment (atomic radii used during the cavity construction R_C = 2.04 Å, R_N = 1.86 Å, R_S = 2.16 Å, R_O = 1.824 Å, R_H = 1.32 Å). DEF2-TZVP functions[7] were employed on all atoms for the description of KS orbitals and electron density. In order to obtain converged results, fine integration grids activated through the DEFGRID3 keyword were used as well as VERYTIGHTSCF convergence criteria in the computation of exchange coupling constants.

Structural models of the dyads **1**, **1ph**, **2** and **3**, replacing the long N-alkyl PDI moiety with a N-CH_3 group to reduce computational complexity, were built and optimized in the closed-shell ground state at which vertical excitation energies were computed. In respect to a previous DFT study of dyad **4** carried out by some of us, where a combined CAM-B3LYP/B3LYP methodology was employed and justified by the perpendicular orientation of the π-systems, i.e. negligible configurational mixing, of the PDI and TAHEL/bridge fragment,[1] we take this occasion to further scrutinize and refine the computational protocol on the basis of the full series of dyads featuring varying bridge length and chemistry. We apply the state-specific ΔSCF approach for the description of the CT states, while local excitations are treated using the spin-flip Tamm-Dancoff approximation (TDA) of time-dependent DFT. The ΔSCF methodology allows to variationally converge on the non-aufbau occupation of the spatially separated D and A orbitals for an accurate description of the CT excited states which are known to be problematic, in general, for standard TD-DFT,[8] i.e., when non-orthogonality between the donorand acceptor orbital involved is present.[9,10] We found the choice of maximum-overlap method (MOM)[11] vs. projected MOM[12] to reliably track the desired electronic state to be highly system and CT state dependent. In the present case, we have further found a significant underestimation of CT state stabilization through solvent effects within linear-response PCM evaluated during the TD-DFT calculation, owing to the long-distance rearrangement of the electron density with respect to the closed-shell reference ground state. We justify the choice of the spin-flip formulation of TDA over conventional TDA with its enhanced performance for the description of the *PDI open-shell singlet which is the lowest lying state within the B_{3g} irreducible

representation (irrep) of the d_{2h} pseudo-symmetry of the PDI fragment. Using the CAM-B3LYP exchange-correlation functional approximation, this computational protocol yields the correct state ordering, ^{1*}PDI > CT_2 > CT_1, in agreement with experimental findings from transient absorption spectroscopy, while applying conventional (spin-conserving) TDA for the description of the ^{1*}PDI yields state ordering which excludes CT_2 from the photophysical pathway, CT_2 > ^{1*}PDI > CT_1 (see Figure S1). Applying conventional TDA also to the CT states leads to a stark overestimation of their respective vertical excitation energy (see Figure S19), owing to the reasons discussed above. In comparison, the CAM-B3LYP/B3LYP methodology[1] yields a qualitatively equivalent state ordering for all dyads with the only exception that the CT_3 shifts below ^{1*}PDI state in dyad 3 owing to a general enhanced CT state stabilization obtained within the B3LYP exchange-correlation functional approximation. This is also reflected in the ordering of the frontier orbitals involved in the photophysics (see Figure 3). The order is preserved throughout the series in case of the CAM-B3LYP, but features a swap of HOMO-3 (*PDI) with HOMO-4 (CT_3) in case of B3LYP.

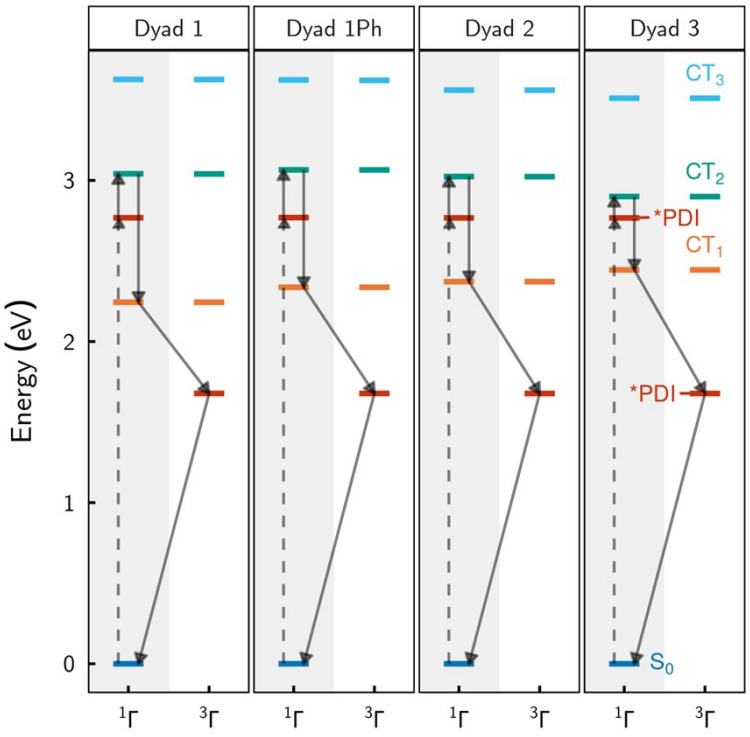

Figure S18. Energy level diagram of dyads **1**, **1ph**, **2** and **3** employing conventional TDA for the local excitations and ΔSCF for the CT_n states.

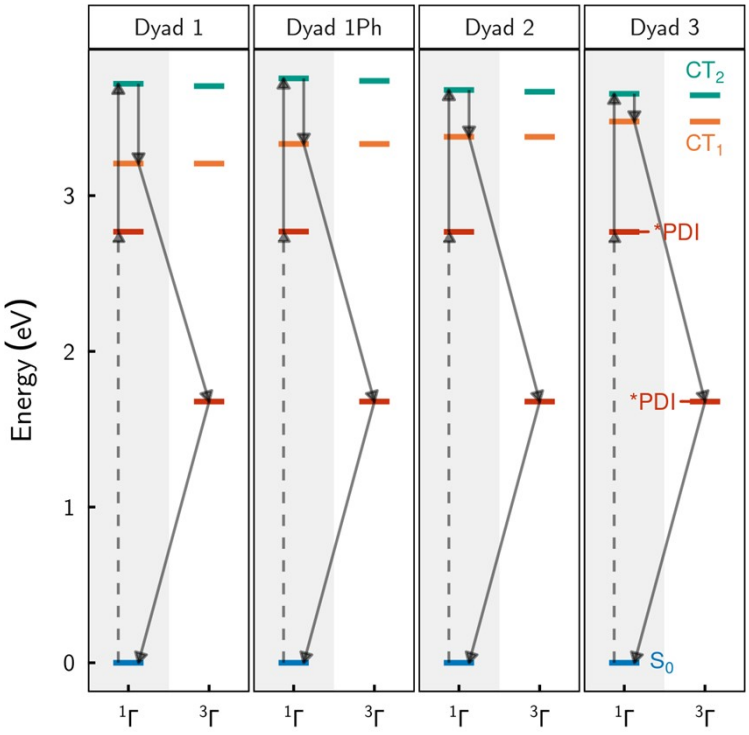

Figure S19. Energy level diagram of dyads **1**, **1ph**, **2** and **3** employing conventional TDA for all excited states.

The exchange coupling constant J in the $JS_A \cdot S_D$ spin Hamiltonian convention was computed at the S_0 optimized within the broken-symmetry (BS) framework as $J = 2(E_{HS} - E_{BS})$, justified by the low spin-contamination observed for the BS ($\langle S^2 \rangle \approx 1$) and high-spin (HS) state ($\langle S^2 \rangle \approx 2$), respectively. This is the result of vanishing SOMO overlap and further allows us to skip the rigorous variational optimization of the spin-adapted open-shell singlet employed in the methodologically related ROKS/PCM approach by Kunze and coworkers.[13] The convergence to a unique, fully localized BS state was verified by employing different initial guess KS orbitals: the appropriately rotated (i) closed-shell ground or (ii) optimized triplet CT state orbitals under exchange of the SOMO from the alpha to the beta channel or (iii) a localized initial guess prepared by the BS facilities provided by ORCA. All three cases converged to the same state.

The absorption spectrum of dyad **1** (see Figure S21, virtually indistinguishable results were obtained for the remaining dyads) was simulated employing the vertical gradient approximation implemented in the ORCA ESD module, where the ground state Hessian is used for both ground and excited state potential energy surfaces along with the vertical excitation energy and vertical excited state gradient to estimate their relative shift in energy and nuclear coordinate space, respectively. The adequate

reproduction of the $S_0 \rightarrow {}^{1*}$PDI band in terms of the 0-0 transition energy and vibronic features serves as a further validation of the current methodology; while the obtained adiabatic energy difference of 2.88 eV (exp: 2.35 eV) suggests a slight overestimation of the vertical separation of the S_0 and ^{1*}PDI potential energy surface (PES), the correct simulation of the vibronic fine structure, reflecting the Franck-Condon factors of distinct vibronic transitions, suggests an accurate description of PES displacement in nuclear coordinate space, opening doors for future efforts to simulate nonadiabatic CT dynamics. In comparison, the CAM-B3LYP/B3LYP approach yields a closer reproduction of the adiabatic energy difference of 2.27 eV as shown in Figure S4.

The Gibbs free energy of the fully charge-separated CT_1 state was computed based on explicitly computed optimized geometry (including vibrational, translational and rotational enthalpic and entropic contributions) and referenced to the S_0 state. The electron affinity (EA) and ionization potential (IP) free energies $^{\Delta G_{EA/IP}}$ leading from the neutral PDI and TAHEL to the singly and doubly reduced and oxidized species, respectively, were obtained from explicitly optimized structures of the PDI and TAHEL fragments and referenced to the S_0 state of the neutral species. To recover the highest possible point group symmetry, we employed the N-H substituted PDI (D_{2h}) and replaced the methyl group along the (pseudo-)C_2 axis of TAHEL with a hydrogen atom, yielding D_{2h} and C_2 symmetry, respectively. The ground state of the singly reduced/oxidized species is a spin doublet while both the closed-shell singlet and the triplet state were considered in case of the doubly reduced/oxidized species. According to the $^{\Delta G_{EA/IP}}$ values presented in Table S1, the closed-shell singlet corresponds to the ground state of both the doubly reduced PDI and doubly oxidized TAHEL species. Notable, in case of the latter, an extremely low-lying triplet state is obtained for the open-shell case owing to the near degeneracy between the HOMO (irrep=b) and HOMO+1 (irrep=a) of the neutral TAHEL.

Table S1. Ionic radius of PDI and TAHEL fragments determined as (i) the distance r between the center of the respective fragment, i.e. midpoint of the central PDI phenyl ring or TAHEL nitrogen, to

the PDI nitrogen or TAHEL para-methylated aromatic carbon, respectively, and (ii) the root mean square distance of all aromatic atoms to the center of the fragment also known as their radius of gyration R_{gyr}. Free energy of the first $\Delta G_{EA/IP}^{1st}$ and second $\Delta G_{EA/IP}^{2nd}$ reduction/oxidation. For the latter we considered both closed-shell singlet (S_0) and possible open-shell triplet (T) ground states.

	r / Å	R_{gyr} / Å	$\Delta G_{EA/IP}^{1st}$ / eV	$\Delta G_{EA/IP}^{2nd,S_0}$ / eV	$\Delta G_{EA/IP}^{2nd,T_1}$ / eV
PDI	5.6	3.5	-3.45	-5.34	-3.95
TAHEL	4.2	2.3	5.69	13.62	13.72

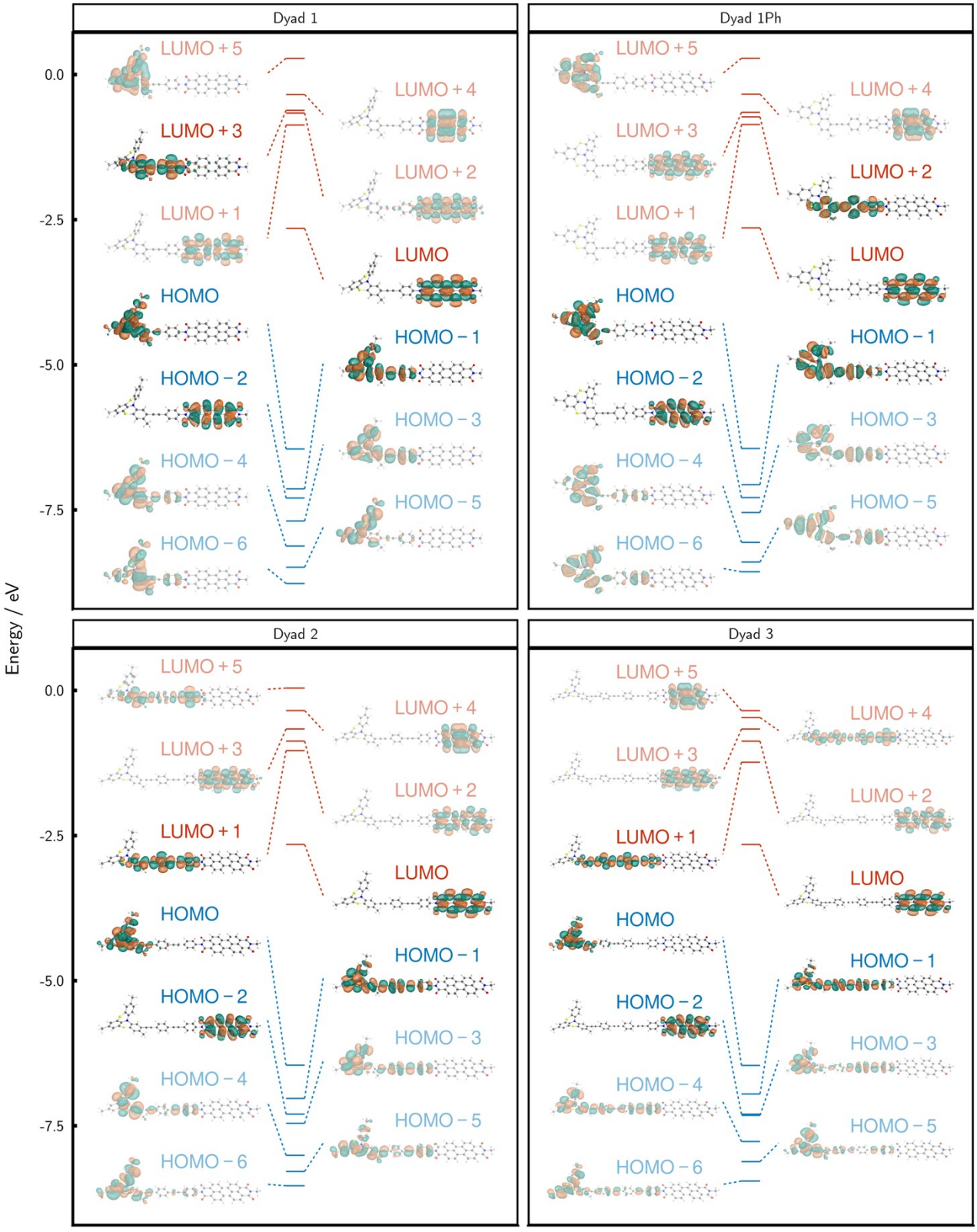

Figure S20. CAM-B3LYP frontier orbitals (iso-value = 0.015) of the closed shell singlet ground state of dyads **1**, **1ph**, **2** and **3**. Orbitals involved in the photophysical pathway *PDI, CT_2, CT_1 (HOMO-2, HOMO-1, HOMO→LUMO) and the lowest lying *TAHEL excited state (HOMO→LUMO+n) are highlighted.

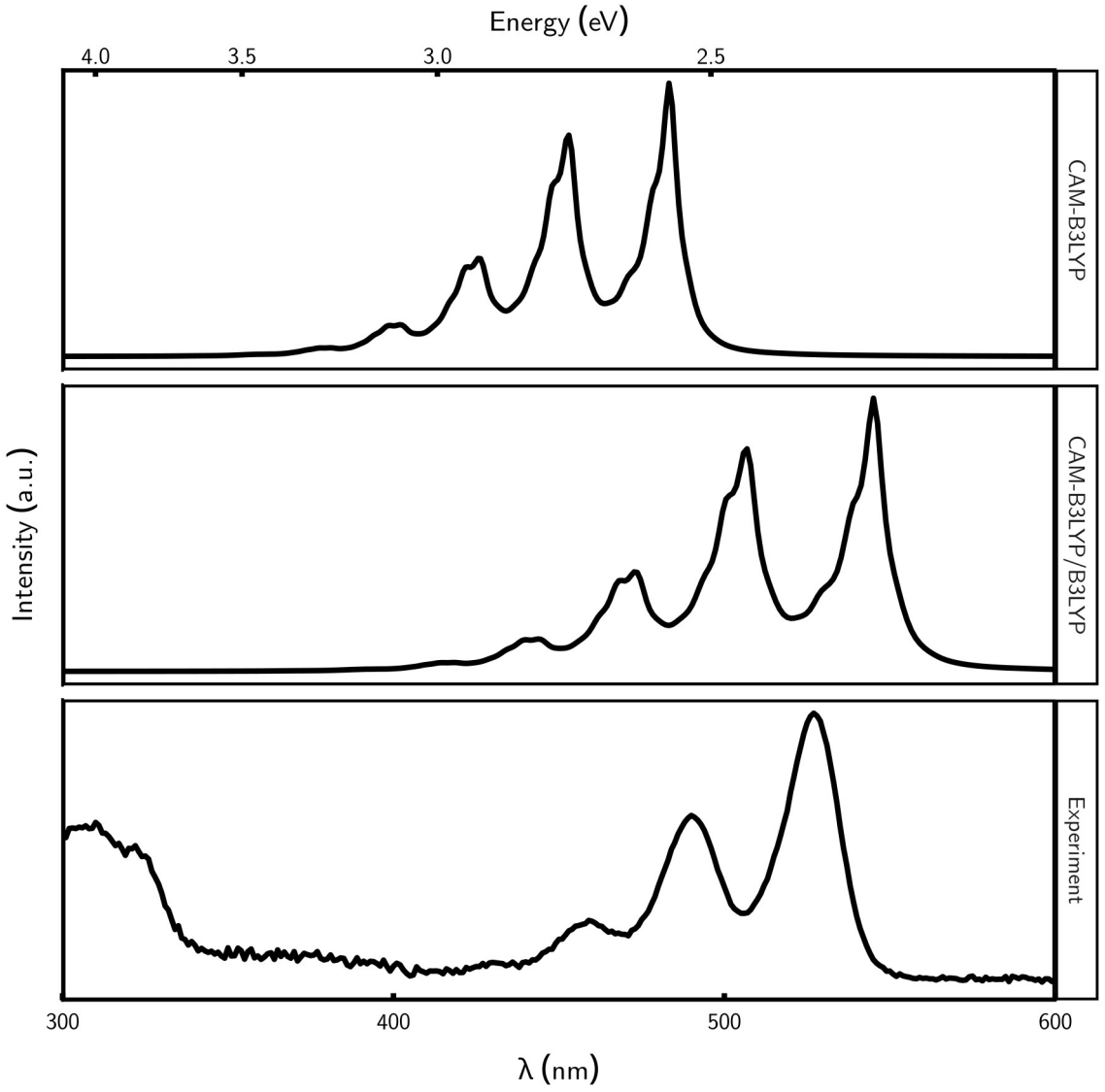

Figure S21. Simulated $S_0 \rightarrow {}^{1*}$PDI absorption band (Lorentzian line broadening: 100 cm^{-1}) of dyad **1** using the current CAM-B3LYP and the previous CAM-B3LYP/B3LYP[1] methodology compared to the experimental absorption spectrum.

S4. Transient absorption spectroscopy

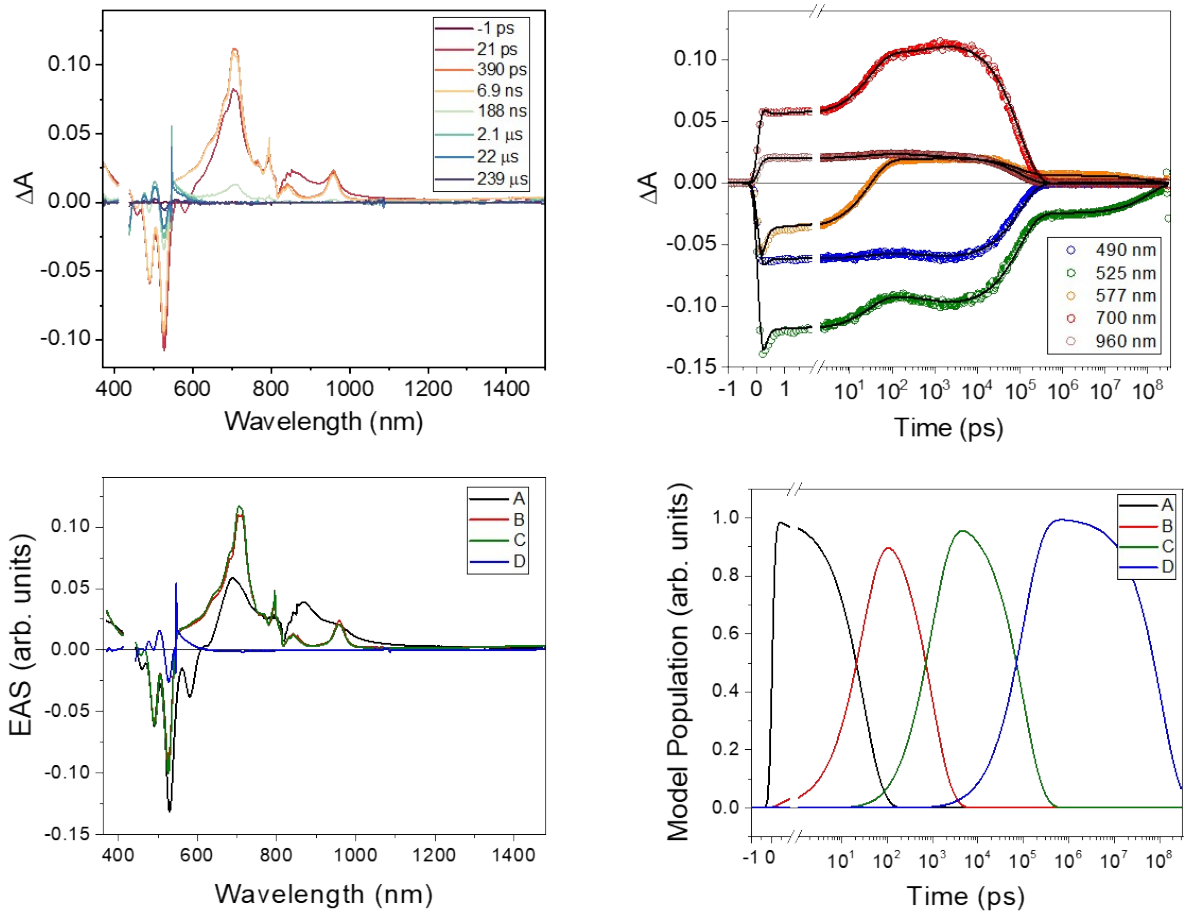

Figure S22. (a) Room-temperature fs/nsTA spectra of **dyad 1ph** in toluene excited at 527 nm and recorded at selected delay times. (b) Selected wavelength kinetic fits, (c) evolution-associated spectra (EAS) and (d) population dynamics obtained by globally fitting the fs/nsTA data. The mechanism assumed to fit the data is A → B → C → D → ground state, where state A represents the singlet excited state of PDI, B is the unrelaxed charge transfer state, C is the fully relaxed charge transfer state, and D is the excited triplet state of PDI.

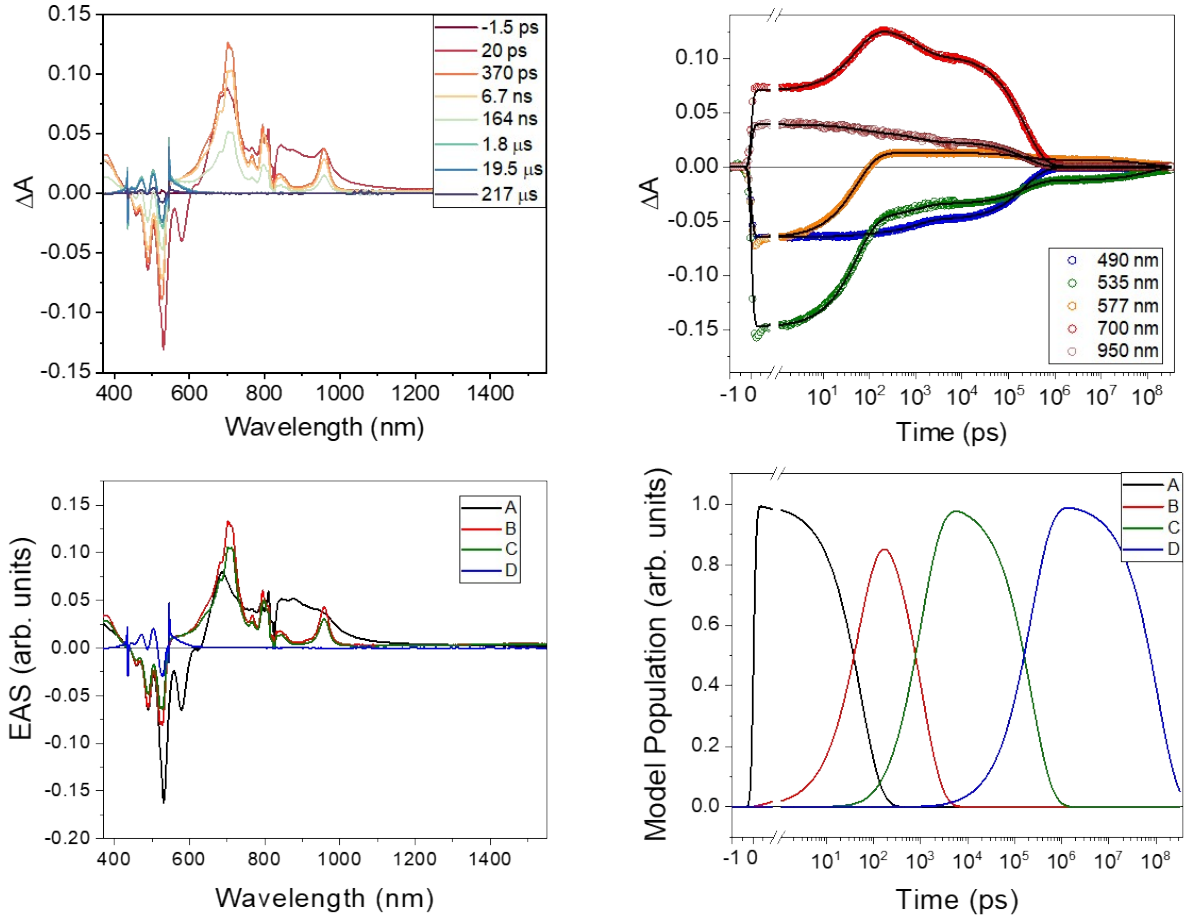

Figure S23. (a) Room-temperature fs/nsTA spectra of **dyad 2** in toluene excited at 527 nm and recorded at selected delay times. (b) Selected wavelength kinetic fits, (c) evolution-associated spectra (EAS) and (d) population dynamics obtained by globally fitting the fs/nsTA data. The mechanism assumed to fit the data is A → B → C → D → ground state, where state A represents the singlet excited state of PDI, B is the unrelaxed charge transfer state, C is the fully relaxed charge transfer state, and D is the excited triplet state of PDI.

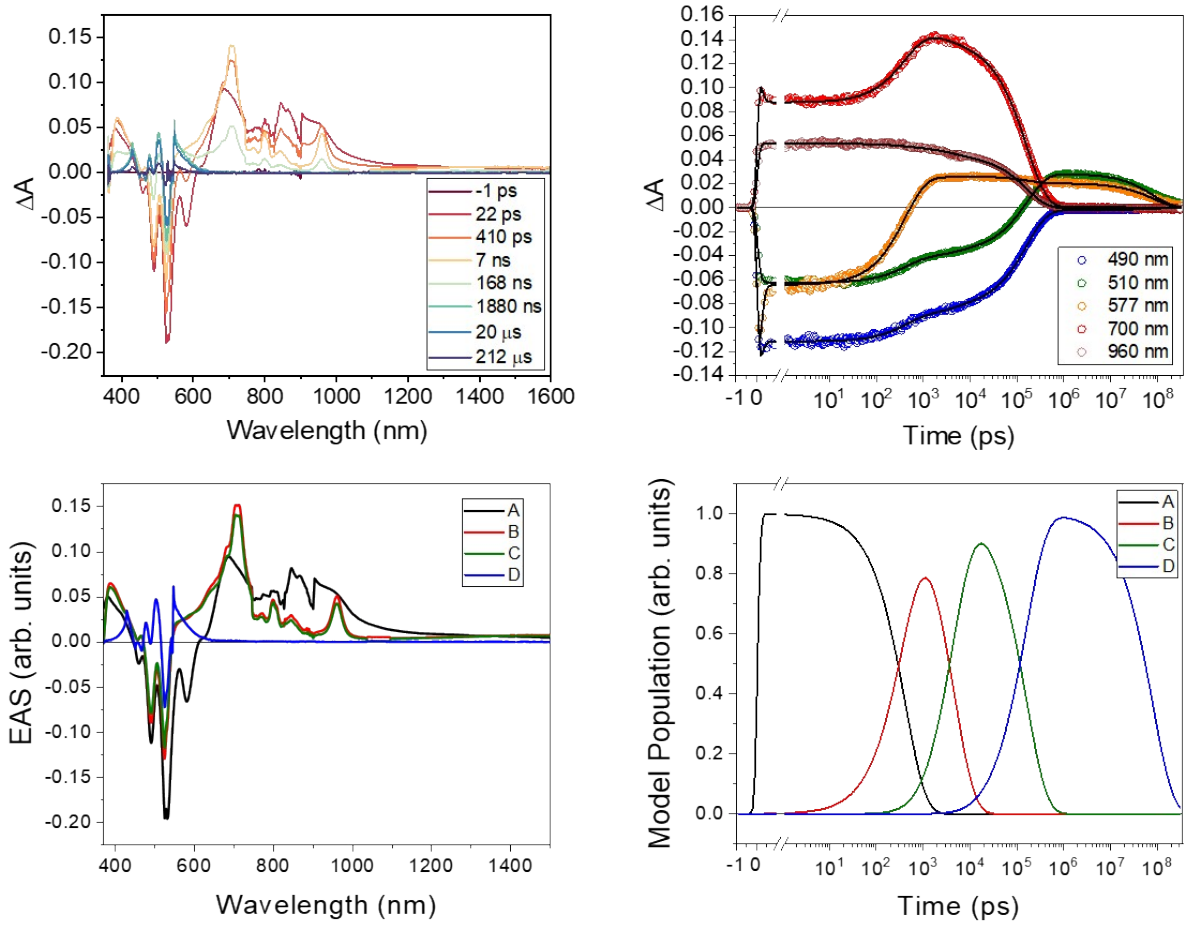

Figure S24. (a) Room-temperature fs/nsTA spectra of **dyad 3** in toluene excited at 527 nm and recorded at selected delay times. (b) Selected wavelength kinetic fits, (c) evolution-associated spectra (EAS) and (d) population dynamics obtained by globally fitting the fs/nsTA data. The mechanism assumed to fit the data is A → B → C → D → ground state, where state A represents the singlet excited state of PDI, B is the unrelaxed charge transfer state, C is the fully relaxed charge transfer state, and D is the excited triplet state of PDI.

S5. Electron Paramagnetic Resonance Spectroscopy

	Mechanism	**[D, E] / MHz**	***Populations***	**Linewidth / mT**	**weight**
Dyad 1	SOCT-ISC	[1300, -118] ± 10	[0.2 0.8 0] ± 0.1	2.0 ± 0.3	
Dyad 1ph	SOCT-ISC	[1312 -126] ± 10	[0.2 0.8 0] ± 0.1	2.5± 0.3	0.82 ± 0.05
	RP-ISC		[0 1 0] ± 0.1		0.18 ± 0.05
Dyad 2	SOCT-ISC	[1320 -129] ± 10	[0.2 0.8 0] ± 0.1	2.5± 0.3	0.76 ± 0.05
	RP-ISC		[0 1 0] ± 0.1		0.24 ± 0.05
Dyad 3	RP-ISC	[1288, -110] ± 10	[0 1 0] ± 0.1	4.5 ± 0.3	

Table S2. Best-fit simulation values from the TREPR spectral simulation shown in Figure 6. For each sample, the zero-field splitting parameters (D and E) of the triplet states are reported in MHz. Two distinct populating mechanisms are identified: spin-orbit charge transfer intersystem crossing (SOCT-ISC) and radical pair intersystem crossing (RP-ISC), as discussed in the main text. For SOCT-ISC, populations are [p_x p_y p_z], while for RP-ISC populations are [p_{-1} p_0 p_{+1}]. The linewidth is determined considering only Gaussian broadening and is reported in mT.

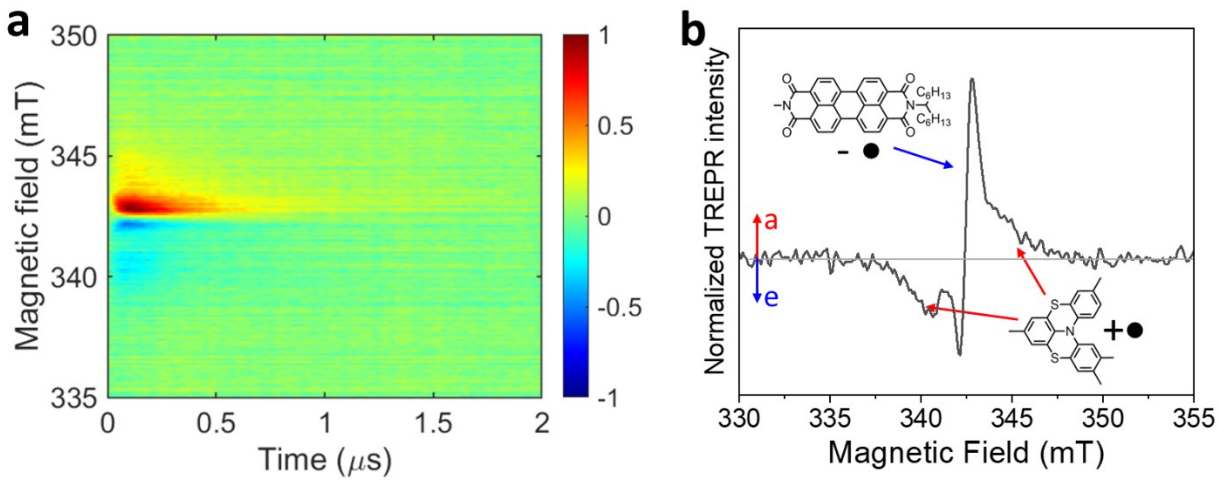

Figure S25. (a) Normalized 2D experimental TREPR contour plots of **dyad 3** in toluene acquired at 85 K after a 527 nm laser pulse (7 ns, 2 mJ). Color legend: red = enhanced absorption, blue = emission, green = baseline. (b) Normalized 1D experimental TREPR spectra taken at 100 ns after the laser pulse (integrated time window = 20 ns). Arrows legend: a = enhanced absorption, e = emission.

S6. Bibliography

(1) Agnoloni, G.; Chiesa, A.; Young, R. M.; Totti, F.; Menichetti, S.; Viglianisi, C.; Wasielewski, M. R.; Carretta, S.; Privitera, A.; Sessoli, R., *J. Am. Chem. Soc.*, 2026, **148**. Accepted.

(2) Xie, J.; Seto, C. T., *Bioorg. Med. Chem.*, 2007, **15** (1), 458–473.

(3) Neese, F., *Wiley Interdiscip. Rev. Comput. Mol. Sci.*, 2012, **2** (1), 73–78.

(4) Neese, F., *Wiley Interdiscip. Rev. Comput. Mol. Sci*., 2025, **15**, e70019.

(5) Yanai, T.; Tew, D. P.; Handy, N. C.,*Chem. Phys. Lett.*, 2004, **393** (1–3), 51–57.

(6) Grimme, S.; Ehrlich, S.; Goerigk, L., *J. Comput. Chem.* 2011, **32** (7), 1456–1465.

(7) Weigend, F.; Ahlrichs, R., *Phys. Chem. Chem. Phys.*, 2005, **7**, 3297–3305.

(8) Selenius, E.; Sigurdarson, A. E.; Schmerwitz, Y. L. A.; Levi, G., *J. Chem. Theory Comput.*, 2024, **20** (9), 3809–3822.

(9) Maitra, N. T., *J. Chem. Phys.*, 2016, **144** (22), 220901.

(10) Dreuw, A.; Head-Gordon, M., *Chem. Rev.*, 2005, **105**, 4009–4037.

(11) Gilbert, A. T. B.; Besley, N. A.; Gill, P. M. W., *J. Phys. Chem. A*, 2008, **112** (50), 13164–13171.

(12) Corzo, H. H.; Abou Taka, A.; Pribram-Jones, A.; Hratchian, H. P., *J. Comput. Chem.,* 2022, **43** (6), 382–390.

(13) Kunze, L.; Hansen, A.; Grimme, S.; Mewes, J. M., *J. Phys. Chem. Lett.*, 2021, **12** (35), 8470–8480.